

Supplementary File for

Observation of novel charge ordering and spin reorientation in perovskite oxide PbFeO₃

Xubin Ye^{1,2,#}, Jianfa Zhao^{1,2,#}, Hena Das^{3,4,#}, Denis Sheptyakov⁵, Junye Yang⁵, Yuki Sakai^{6,3}, Hajime Hojo⁷, Zhehong Liu^{1,2}, Long Zhou^{1,2}, Lipeng Cao¹, Takumi Nishikubo³, Shogo Wakazaki³, Cheng Dong^{1,2}, Xiao Wang⁸, Zhiwei Hu⁸, Hong-Ji Lin⁹, Chien-Te Chen⁹, Christoph Sahle¹⁰, Anna Efiminko¹⁰, Huibo Cao¹¹, Stuart Calder¹¹, Ko Mibu¹², Michel Kenzelmann⁵, Liu Hao Tjeng⁸, Runze Yu^{*,1,2,4}, Masaki Azuma^{*,3,6}, Changqing Jin^{1,2,13}, and Youwen Long^{*,1,2,13}

¹Beijing National Laboratory for Condensed Matter Physics, Institute of Physics, Chinese Academy of Sciences, Beijing 100190, China

²School of Physical Sciences, University of Chinese Academy of Sciences, Beijing 100049, China

³Laboratory for Materials and Structures, Tokyo Institute of Technology, 4259 Nagatsuta, Midori, Yokohama 226-8503, Japan

⁴Tokyo Tech World Research Hub Initiative (WRHI), Institute of Innovative Research, Tokyo Institute of Technology, 4259 Nagatsuta, Midori-ku, Yokohama, Kanagawa 226-8503, Japan

⁵Laboratory for Neutron Scattering and Imaging, Paul Scherrer Institut, CH-5232 Villigen, Switzerland

⁶Kanagawa Institute of Industrial Science and Technology, 705-1 Shimoimaizumi, Ebina 243-0435, Japan

⁷Department of Advanced Materials and Engineering, Faculty of Engineering Sciences, Kyushu University, Kasuga 816–8580, Japan

⁸Max-Planck Institute for Chemical Physics of Solids, Nöthnitzer Straße 40, 01187 Dresden,

Germany

⁹National Synchrotron Radiation Research Center, 101 Hsin-Ann Road, Hsinchu 30076, Taiwan,

R.O.C

¹⁰European Synchrotron Radiation Facility, 71 Avenue des Martyrs, 38043 Grenoble, France

¹¹Neutron Scattering Division, Oak Ridge National Laboratory, Oak Ridge, Tennessee 37831,

United States

¹²Graduate School of Engineering, Nagoya Institute of Technology, Nagoya 466-8555, Japan

¹³Songshan Lake Materials Laboratory, Dongguan, Guangdong 523808, China

#These authors contribute equally to this work.

*Corresponding email: ywlong@iphy.ac.cn (Y.W.L.); yurz@iphy.ac.cn (R.Z.Y.); and mazuma@msl.titech.ac.jp (M.A.)

Supplementary Table S1 | Crystallographic parameters of PbFeO₃ refined from SXRD pattern at RT^a

atom	site	x	y	z	100×B _{iso} (Å)
Pb1	4c	0	-0.0037(1)	0.25	0.78(1)
Pb2	4c	0	0.4996(1)	0.25	0.78(1)
Pb3	4c	0	0.8282(1)	0.25	0.78(1)
Pb4	4c	0	0.1546(1)	0.25	0.78(1)
Pb5	4c	0	0.3349(1)	0.25	0.78(1)
Pb6	4c	0	0.6593(1)	0.25	0.78(1)
Fe1	8d	0.25	0.25	0	0.22(2)
Fe2	16h	0.2558(6)	0.5840(1)	0.9993(6)	0.22(2)
O1	8g	0.301(4)	0.7756(8)	0.25	1.8(3)
O2	16h	0.308(2)	0.6732(7)	0.053 (2)	1.8(3)
O3	8f	0	0.2703(9)	-0.064(4)	1.8(3)
O4	8e	0.277(4)	0	0	1.8(3)
O5	8f	0	0.0763(10)	1.050(4)	1.8(3)
O6	8g	0.187(4)	0.5869(8)	0.25	1.8(3)
O7	8f	0	0.6082(9)	-0.038 (4)	1.8(3)
O8	8g	0.283(4)	0.4047(7)	0.25	1.8(3)

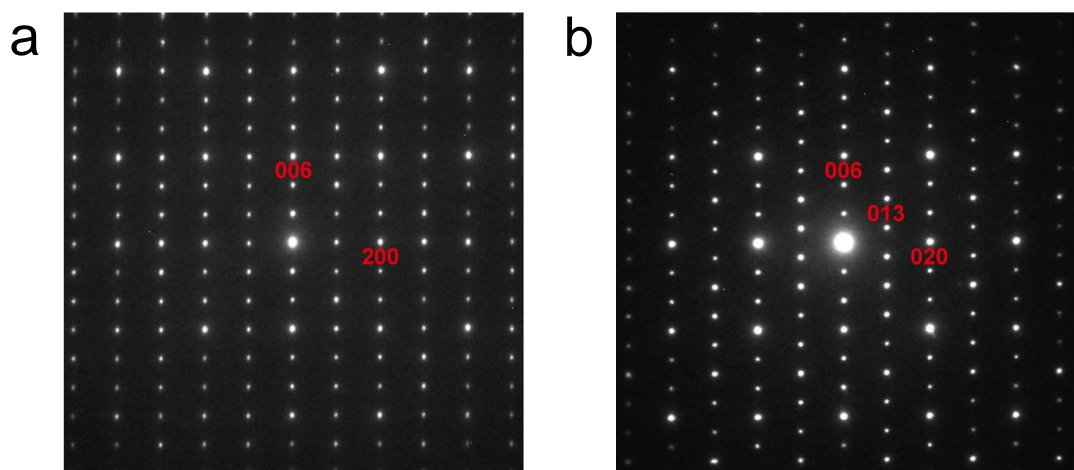
^aSpace group *Cmcm* (No. 63), *Z* = 24. *a* = 7.88504(2) Å, *b* = 23.37741(8) Å, *c* = 7.70905(2) Å, $\rho_{\text{cal}} = 8.723(1)$ g/cm³, *V* = 1421.023(1) Å³. *R*_{wp} = 7.63%, *R*_p = 5.30%, χ^2 = 9.20.

Supplementary Table S2 | Pb-O and Fe-O bond lengths and BVSs for PbFeO₃
Refined from SXRD pattern at RT.

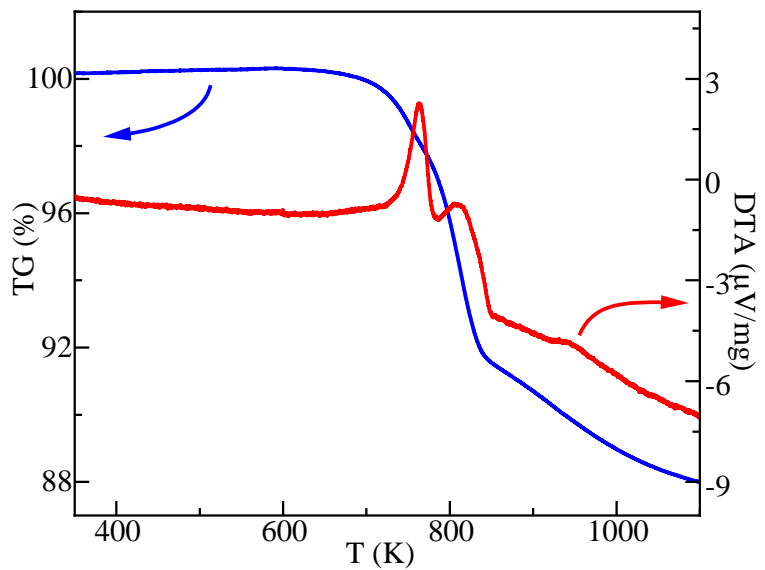
	Distance (Å)	Average bond length (Å)	BVS
Fe1-O	1.897(2) × 2	2.014	3.03
	2.058(2) × 2		
	2.087(3) × 2		
Fe2-O	1.952(3)	2.032	2.87
	1.973(3)		
	1.981(2)		
	2.009(3)		
	2.115(2)		
Pb1-O	2.427(4) × 2	2.771	1.94
	2.738(6) × 2		
	2.866(6) × 4		
	2.912(6) × 2		
Pb2-O	2.516(4) × 2	2.778	2.01
	2.611(5) × 4		
	3.005(6) × 2		
	3.148(6) × 2		
Pb3-O	2.475(5) × 2	2.774	2.23
	2.675(5) × 2		
	2.712(6) × 2		
	2.786(3) × 4		
	3.213(3) × 2		
Pb4-O	2.189(4) × 4	2.588	3.72
	2.395(5) × 2		
	2.933(4) × 2		
	3.235(6) × 2		
Pb5-O	2.092(4) × 2	2.455	3.93
	2.107(4) × 2		
	2.767(6) × 2		
	2.853(5) × 2		
Pb6-O	2.182(4) × 2	2.541	3.52
	2.245(6) × 2		
	2.521(4) × 2		
	2.880(4) × 4		

Supplementary Table S3 | Peak area ratio for each peak and calculated average Pb valence for HAXPES data.

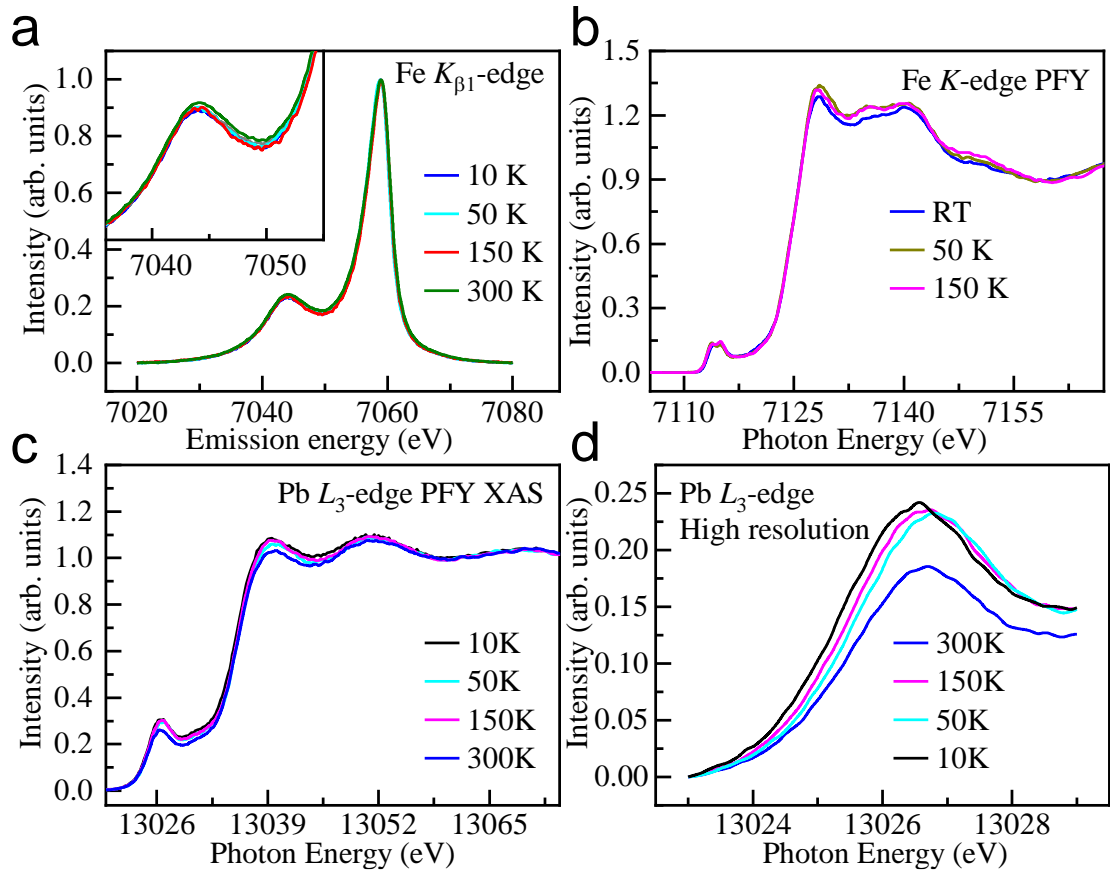
	$4f_{5/2}$		$4f_{7/2}$	
PbCrO ₃	0.61	0.39	0.61	0.39
PbFeO ₃	0.59	0.41	0.58	0.42
PbCoO ₃	0.48	0.52	0.45	0.55



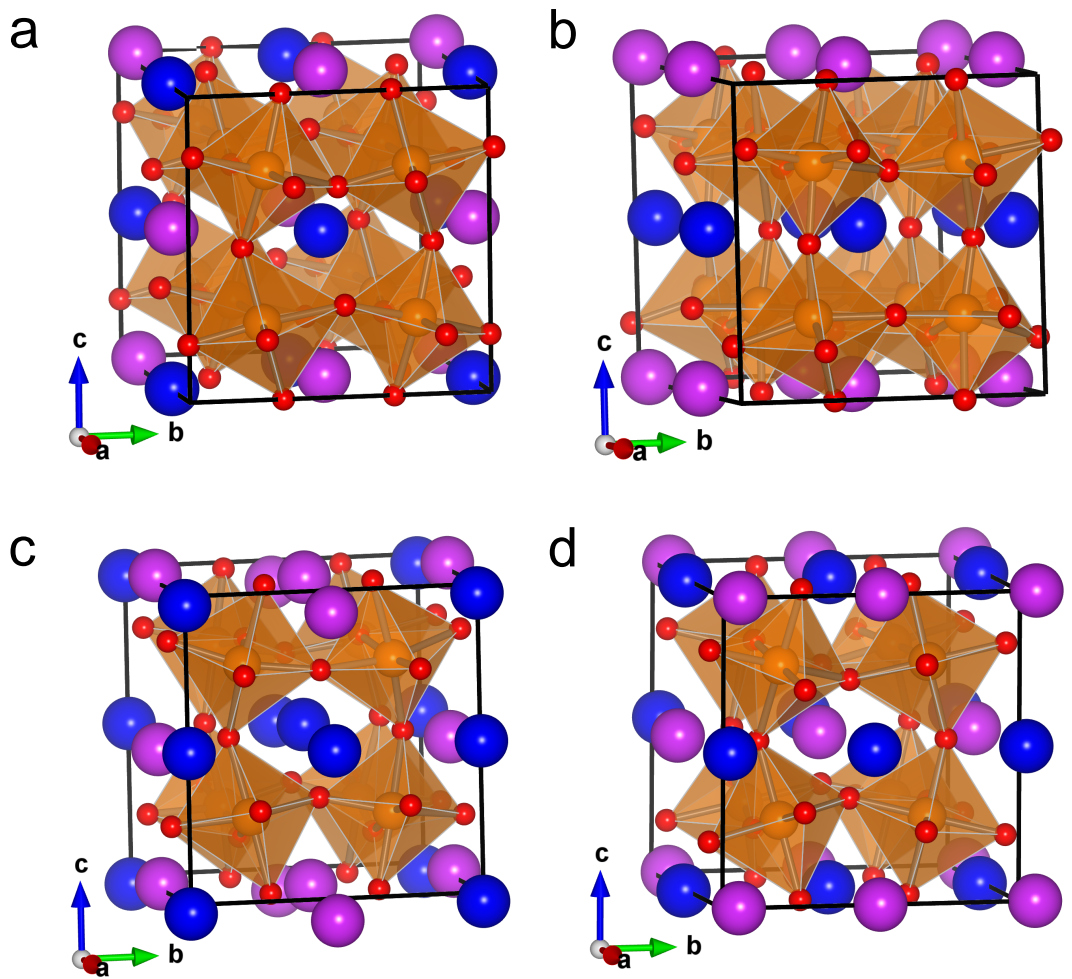
Supplementary Figure S1 | ED patterns along the pseudocubic zone axis at RT for PbFeO_3 . (a) [100] and (b) [001] axis. Multiple scattering effects make it possible to observe $h00$ reflections with $h = \text{odd}$ at [010].



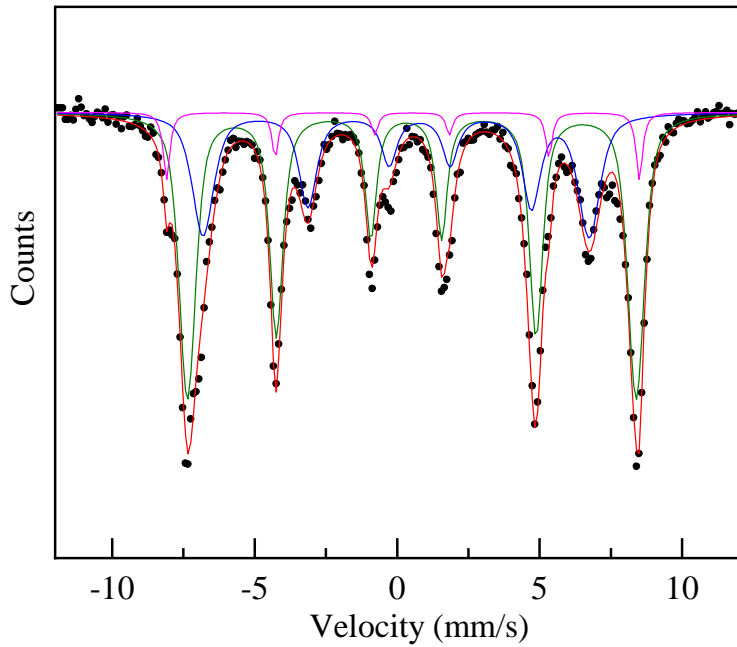
Supplementary Figure S2 | Temperature dependence of thermogravimetry (TG) and differential thermal analysis (DTA) for PbFeO_3 .



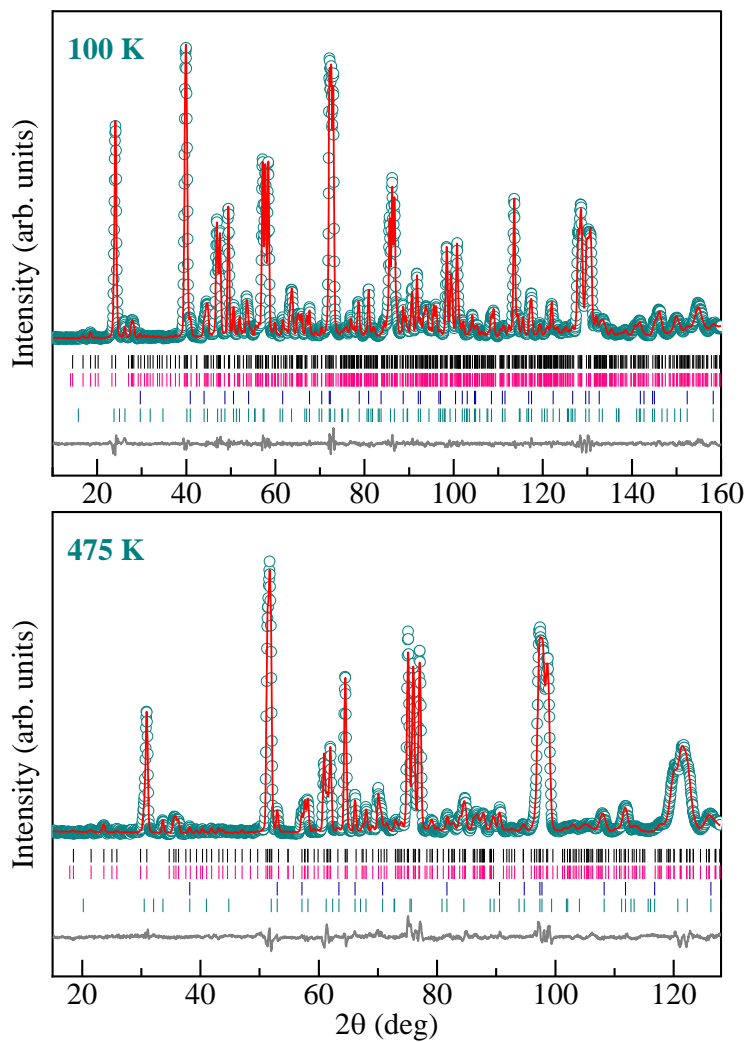
Supplementary Figure S3 | Temperature dependent XAS measurement for PbFeO_3 . (a) Fe $K_{\beta 1}$ -edge for PbFeO_3 . (b) Fe K -edge for PbFeO_3 in PFY model. (c) Pb L_3 -edge for PbFeO_3 in PFY model. (d) High resolution Pb L_3 -edge for PbFeO_3 .



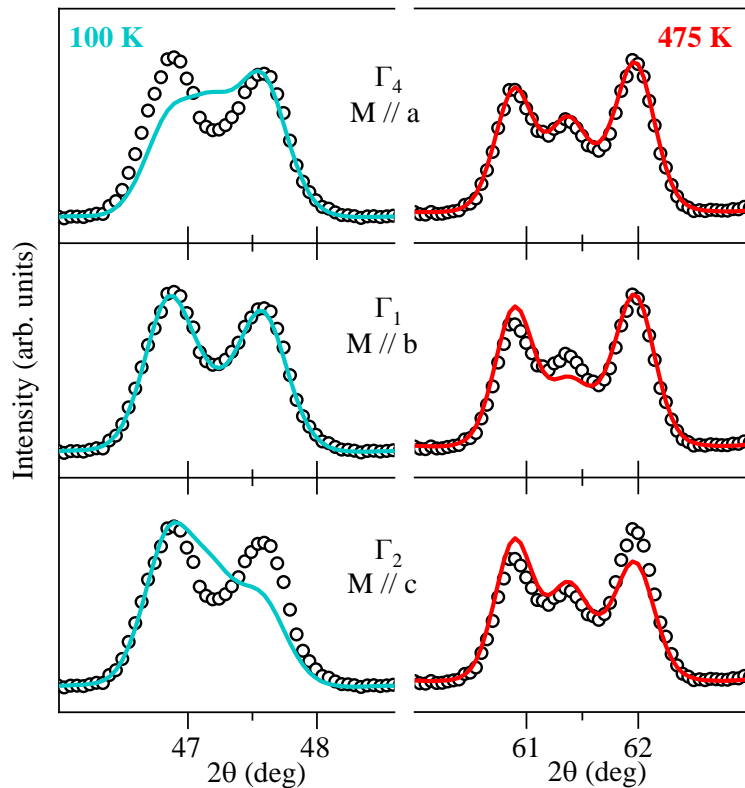
Supplementary Figure S4 | Represents the $\text{Pb}^{2+}/\text{Pb}^{4+}$ for different charge-order phases. (a) rock-salt (Cm), (b) layered (Pc), (c) mixed (Pm) and (d) columnar ($Pmmn$).



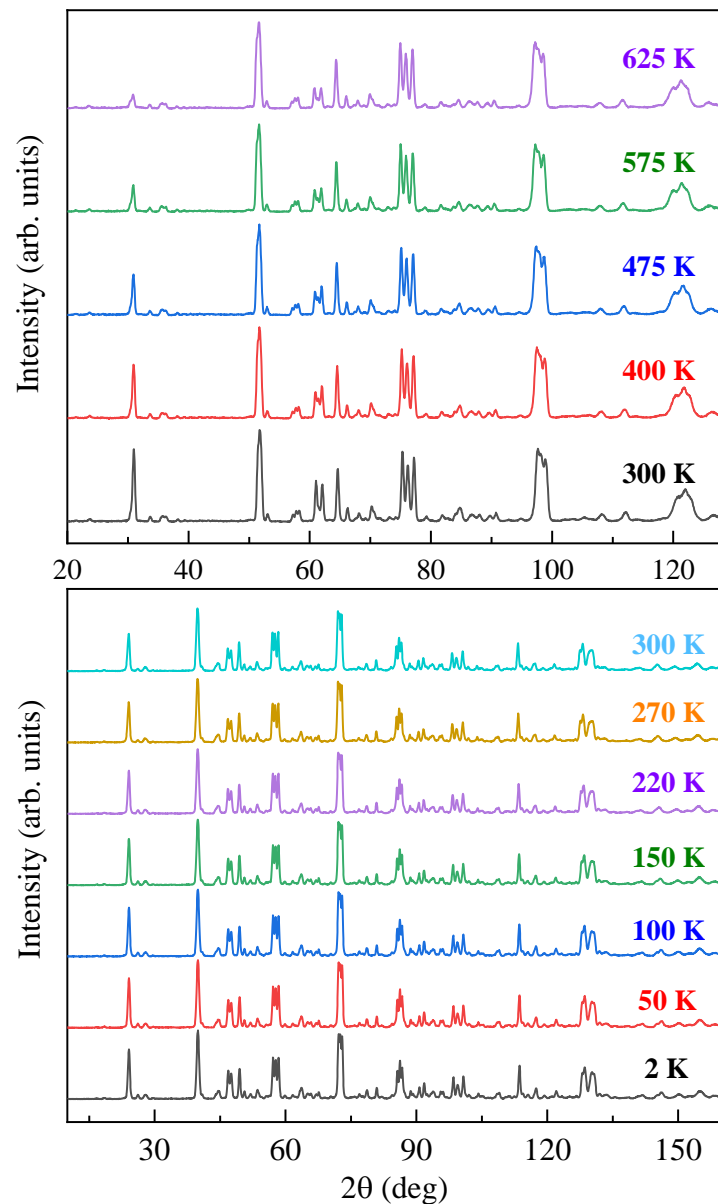
Supplementary Figure S5 | Mössbauer spectrum for the ^{57}Fe -enriched powder sample at 300 K. The spectrum can be fitted with three sets of magnetically-split sextets, which are attributed to Fe at the $16h$ site (olive, 60%), $8d$ site (blue, 34%), and at $\alpha\text{-Fe}_2\text{O}_3$ impurities (pink, 6%).



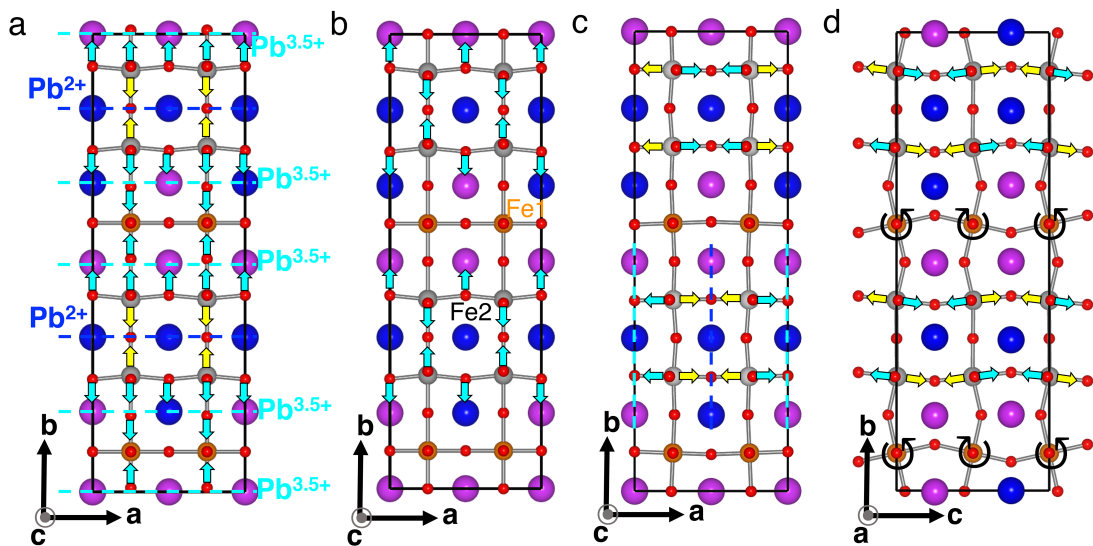
Supplementary Figure S6 | The NPD patterns and the refinement results at 100 K and 475 K for PbFeO_3 . The observed (dark cyan circles), calculated (red line), and difference (dark gray) values are shown. The ticks correspond to the allowed nuclear (black), magnetic (pink) Bragg peaks of PbFeO_3 and allowed nuclear (navy), magnetic (green) Bragg reflections of the impurity phase Fe_2O_3 (~5 wt %), respectively.



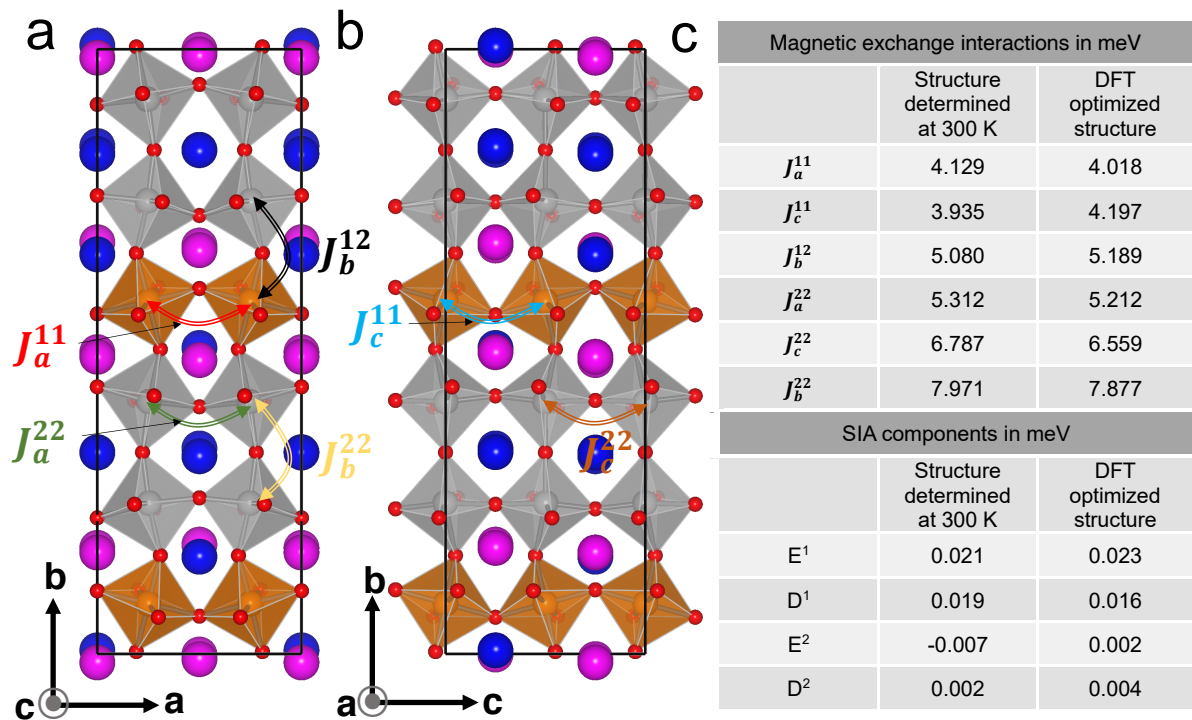
Supplementary Figure S7 | Magnetic Bragg peaks and the fitting curves using the three different spin models at 100 K (left panel) and 475 K (right panel) for several characteristic peaks of NPD patterns of PbFeO_3 . The gray balls and solid curves correspond to measured data and fitted results, and three spin models (Γ_4 , Γ_1 and Γ_2) are represented from up to down, respectively.



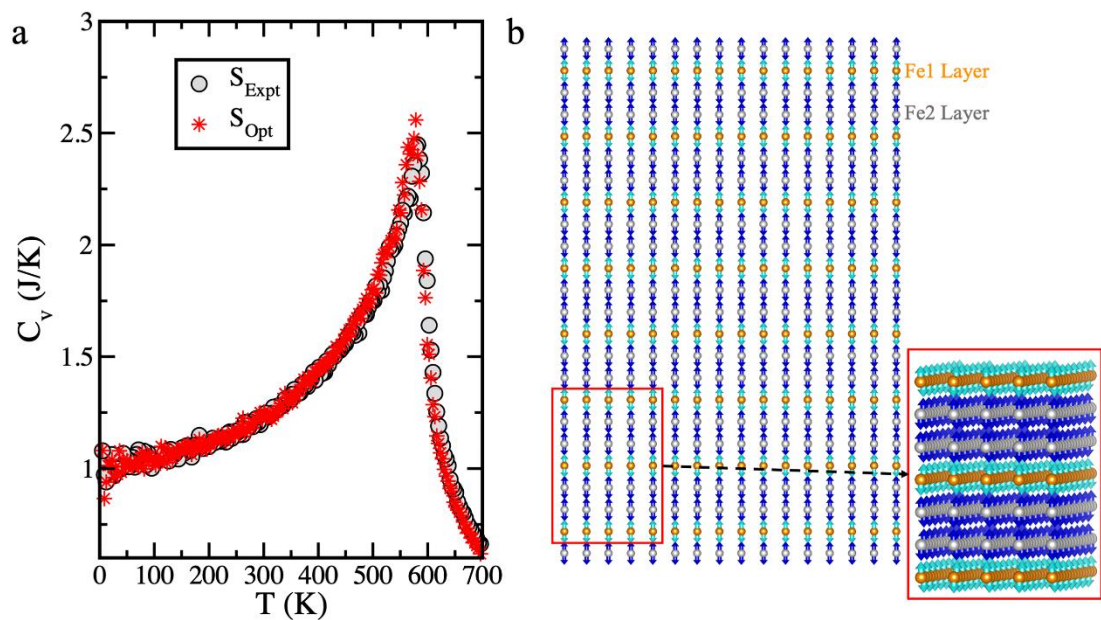
Supplementary Figure S8 | The NPD patterns measured at 2 - 625 K for PbFeO_3 .



Supplementary Figure S9 | Symmetric distortions which owe their origin to the special arrangements of Pb cations. The symmetric distortions that correspond to DT1 (transforms $Pm\bar{3}m \rightarrow P4/mmm$, (a)), DT2 (transforms $Pm\bar{3}m \rightarrow Pmmm$, (b)), Z4 (transforms $Pm\bar{3}m \rightarrow Cmmm$, (c)) and Z4 (transforms $Pm\bar{3}m \rightarrow Pmma$, (d)). Blue and cyan layers represent average 2+ and 3.5+ oxidation state of Pb ions, respectively. The Fe and oxygen movements are denoted by yellow and cyan arrows, respectively. The in-phase oxygen octahedra rotations at the Fe1 layers around a axis is denoted by black arrow.

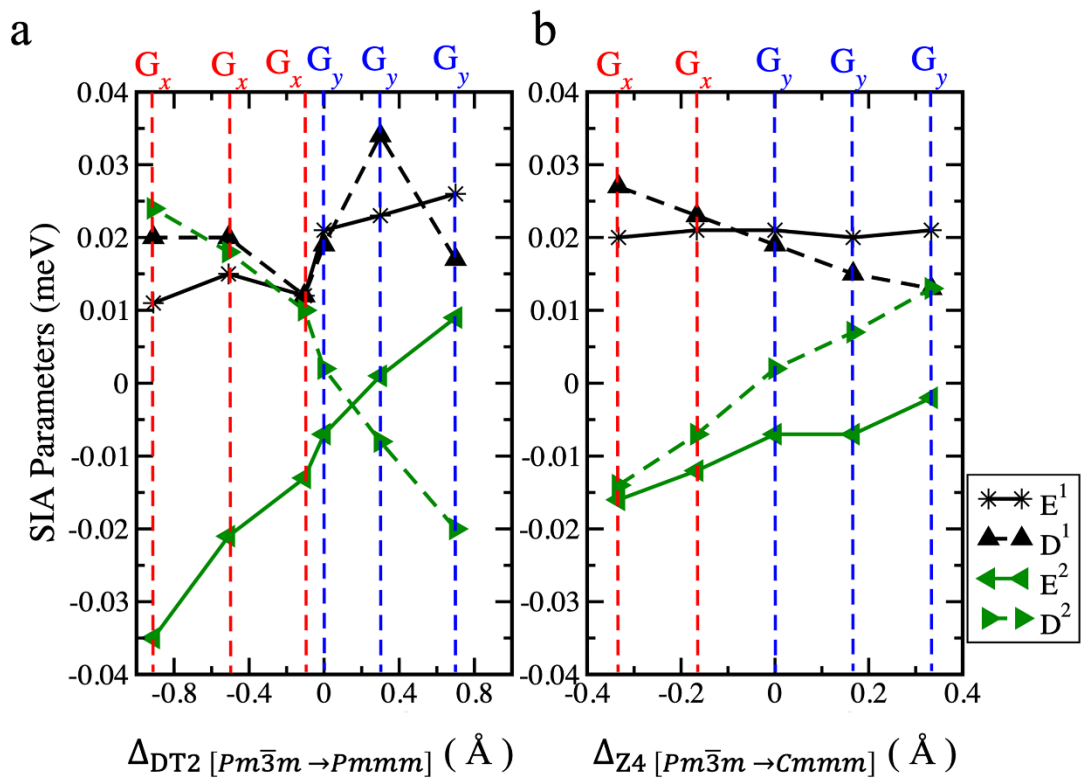


Supplementary Figure S10 | Parameterize the spin Hamiltonian. (a) and (b) Superexchange interaction paths between Fe spins. (c) Estimated values of the symmetric exchange interactions between Fe spins and single ion magnetic anisotropy energies of Fe1 (E^1 and D^1) and Fe2 (E^2 and D^2) ions.



Supplementary Figure S11 | Results of finite temperature Monte Carlo simulations.

(a) Exhibits magnetic phase transition ~ 580 K for both S_{Expt} and S_{Opt} structures. (b) Denotes the G -type (G_y) antiferromagnetic structure at 20 K. The cyan and blue arrows represent Fe1 and Fe2 spins, respectively.



Supplementary Figure S12 | Stability of various magnetic phases as modulation of structural distortions. (a) and (b) Estimated single ion anisotropy (SIA) parameters associated with Fe1 (E^1 and D^1) and Fe2 (E^2 and D^2) magnetic sublattices as a function of $DT2$ ($Pm\bar{3}m \rightarrow Pmmm$) and $Z4$ ($Pm\bar{3}m \rightarrow Cmmm$) distortions, respectively. The magnetic phases stabilized in the Monte Carlo simulations considering the estimated SIA parameters below the magnetic phase transition are also shown.